C. R. Mecanique 341 (2013) 65–74

Contents lists available at SciVerse ScienceDirect

Comptes Rendus Mecanique

www.sciencedirect.com

Combustion, flow and spray dynamics for aerospace propulsion

Large eddy simulation of a monocomponent spray evaporating in a heated and turbulent flow

Virginel Bodoc *, Olivier Rouzaud, Gerard Lavergne

ONERA – The French Aerospace Lab, 31055, Toulouse, France

ARTICLE INFO

Article history:
Available online 8 January 2013

Keywords:
Turbulent flow
Droplet evaporation
Large eddy simulation

ABSTRACT

Different experimental and numerical works were conducted at ONERA in order to carry out information about the evaporation of mono and multicomponent droplets. Different models were proposed and tested in computing codes. The goal of this paper is to describe the evaporation of carburant droplets in a highly turbulent and heated flow by numerical simulation. Firstly, the numerical approach is used in the comprehension of the mono and two-phase flow behavior. Secondly, a simple evaporation model implemented in the code CEDRE is tested for this configuration.

1. Introduction

The evaporation phenomenon can be found in a large number of applications such as internal combustion engines, gas turbines, rocket engines or industrial burners. For all these applications, the liquid fuel is injected in the combustion chambers and atomized. Thanks to evaporation, the gaseous mixture is burnt. In most cases, the evaporation has a characteristic time greater than the one of the combustion. Thus, it becomes of great importance to dispose of accurate, flexible and low computational cost evaporation models that can be implemented in CFD codes.

Up to now, at ONERA, experimental investigations and numerical simulations have yielded correlations that can be used for modeling mono- and multicomponent liquids evaporation [1,2]. As a further evaluation step, these evaporation models, implemented in the ONERA's CEDRE code, were applied for more complex configurations. Very satisfactory results were obtained for cooling polydisperse sprays injected in a stagnant atmosphere [3].

The main objective of this paper is to validate a numerical tool simulating the droplet vaporization for a complex configuration using a Large Eddy Simulation (LES) approach. Such a tool is the computing code CEDRE provided with evaporation models. The concerned configuration, reproducing a highly turbulent and heated flow, had already been experimentally described [4,5]. M. Cochet [4] has investigated the vaporization of an acetone polydisperse droplets using the Planar Laser Induced Fluorescence (PLIF) system. Later, in order to evaluate the fuel vaporization, V. Bodoc and F. Moreau [6] measured the droplets temperature, size and velocity for mono and bi-component liquids. A part of the experimental database will be used in the present study for comparison with the numerical results.

The application of RANS models to account for the turbulence is well adapted for some simple configurations like droplets emerging at low velocity in a stagnant atmosphere. Nevertheless, for real environments (as the present configuration) the unsteady anisotropic flows need to be studied in the frame of a large eddy simulation approach.

* Corresponding author.
E-mail addresses: Virginel.Bodoc@onera.fr (V. Bodoc), Olivier.Rouzaud@onera.fr (O. Rouzaud), Gerard.Lavergne@onera.fr (G. Lavergne).

1631-0721/$ – see front matter
http://dx.doi.org/10.1016/j.crme.2012.10.007

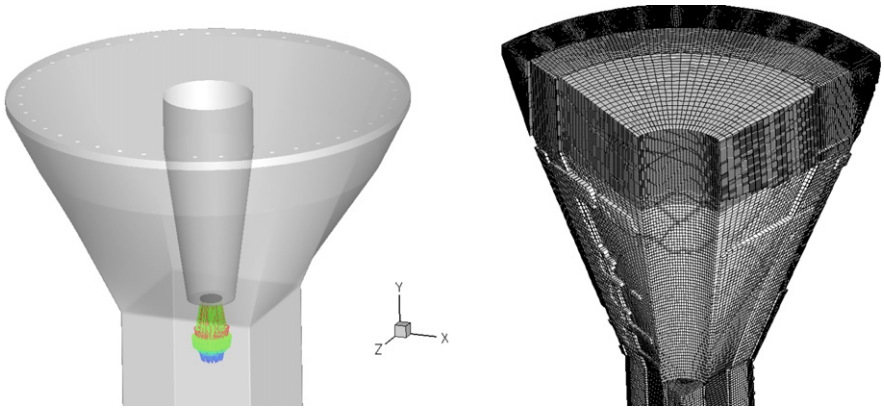

Fig. 1. Left: geometry of the computing domain and the velocity vectors of the injected droplets. Right: a global view of the mesh. Number of cell grids: 6 400 000.

2. The geometry and the grid of the computational domain

Because the experimental configuration was largely described in different references [4–6], within this paper only the essential aspects are introduced. The channel configuration consists of a turbulence generator and a vertical square cross-section channel. The turbulence generator is made of a circular plate perforated by 45 holes of 3 mm diameter and a convergent. The air is injected through the perforations and the developed 45 jets impinge the convergent generating a high turbulence level. According to the works of Cochet [4], the integral length scale is about 25 mm, while the Kolmogorov length scale is about 275 μm. An ultrasound atomizer is placed in the centre of the perforated plate and the nozzle tip is located at the entrance of the square section channel. The atomization process provides droplets with a wide range of diameters and velocities.

The geometry adopted for the numerical simulation corresponds to the experimental configuration except some small modifications which consist mainly in the reduction of the channel length in order to reduce the computational cost. The left side of Fig. 1 shows the geometry of the turbulence generator and the upper part of the investigation channel. The micro-jets inside the turbulence generator are directed downward in the direction parallel to the OY axis.

From the point of view of the liquid phase analysis (droplet heating, evaporation and dispersion), the zone of interest is located in the first part of the square cross section channel. Due to the evaporating properties of the droplets and to the operating conditions (air temperature and the liquid mass flow rate), an important evaporation of droplets occurs within the first 300–350 mm of the channel. Nevertheless, the numerical simulation cannot be performed only for this region because we cannot provide the inlet conditions in the channel due to the lack of experimental data. Hence the entire configuration, including the turbulence generator, needs to be simulated.

The construction of the computational grid represents an important stage in the numerical approach and it is an important factor contributing to the quality of the results. The presence of a large spectrum of geometrical scales, from 3 mm (for the perforations) to 92 mm (for the channel section edge) raised large difficulties in the generation of a quality grid.

The right image from Fig. 1 shows an overall view of the mesh. The unstructured mesh is composed of hexahedral elements. This type of mesh was chosen for two main reasons. The hexahedra are necessary for the application of wall functions but they are also advantageous in terms of the overall number of cells since the near wall grid refinement can easily be controlled by adapting the cells aspect ratio. The skewness of the mesh was examined with the available tools of Gambit and the values found are inferior to 0.8, value which indicates that the cells are not too distorted.

For an efficient and accurate calculation of the turbulent flow, the grid has several refined zones. In order to describe the regions with high turbulence level, a first area with a high refinement is located in the region of impinging jets. Beaubert [7] simulated a plane turbulent jet impinging perpendicularly a surface using a LES approach. He used a number of 160 grid points for a dimensionless distance of 10 (calculated as the ratio of the jet length to the initial diameter) and a Reynolds number based on the jet initial diameter of 3000. Referring to this work, in the present paper, for the same Reynolds number and a dimensionless length of the jet of 7, only 60 computational points were used, their distribution being uniform along the axis of the jet. The number of the computational points was limited for computational costs reasons. Besides, to describe accurately the strong gradient regions, the grid points are clustered near the expected jet.

The square channel inflow area is also of particular interest. For the current simulation, the reduced hight of the first cell is $y^+ \approx 5$. Furthermore, the grid resolution in the volume of the channel was kept at a relatively constant value of 1 mm which is about four times superior to the experimental Kolmogorov length scale. Grid refinement along the axis OY is relaxed downstream in the channel.

The boundary conditions were chosen in order to simulate the conditions of the experimental configuration with the functionalities available in CEDRE. The boundary conditions applied to the gaseous flow are of the subsonic inlet/outlet

type. For the wall boundary isothermal condition is assumed. To avoid a too refined grid within the boundary layer, wall functions are used under the hypothesis of logarithmic profile of velocity in the turbulent boundary layer.

3. Physical and numerical models

3.1. Gaseous phase

Ozdemir et al. [8] have shown that the impingement of a jet on a plate generates unsteady and complex flow. The unsteadiness of such flow has different origins like the vortices caused by the shear layer instability and the unsteady separation which might occur after deflection from the wall. The generation of vortices, the entrainment of the air from the surrounding medium, the impingement of jet and the separation of flow are factors that contribute to the complexity of the flow justifying the use of the LES approach. Since only the large structures of the flow are solved by LES, the small eddies, supposed to be isotropic, are modeled by a sub-grid scale (SGS) model. For this simulation, a standard Smagorinsky model is used to account for the unresolved scales of turbulence.

For the spatial discretization scheme, a second order method based on the calculation of the gradients with a least square technique was used. The fluxes were calculated with a low-Mach number preconditioning method and Van Leer flux limiter. Concerning the temporal evolution, an implicit Runge–Kutta second order scheme was adopted. A constant global time step of 10^{-5} s was used, corresponding to a maximum CFL value of 6 in the region of micro-jets. In the square cross-section channel the CFL number takes a maximum value of 0.02. To account for the acoustical phenomenon, the simulation uses a low-Mach number correction. Among the two types of preconditioning, local and global, the second one was kept because it seemed to be more robust for the given configuration.

3.2. Dispersed phase

For the dispersed phase, the Lagrangian simulation is performed with the so-called numerical particle approach, which consists in gathering a number (*weight*) of physical particles with the same properties (position, size, velocity and temperature) into a numerical droplet. From a practical point of view, the *weight* of the numerical particles is based on the mass inflow rate and keeps a constant value during the numerical particle life time (no secondary break-up is assumed).

The Lagrangian approach is based on the tracking of individual droplets in the gaseous flow field by solving their instantaneous equation of motion in a three-dimensional Cartesian system of coordinates. The other equations describing the behavior of droplets are those corresponding to the mass, momentum and energy conservation. To solve this equation system a semi-analytical scheme is applied using a time step of 10^{-5} s. This value is much inferior to the characteristic times of the droplets. As example, for a droplet of 20 μm the response time is 0.001 s and the temperature relaxation time is about 0.0015 s.

The considered forces acting on the droplet are only the drag and gravity forces. The evaporation is modeled with the infinite conduction model because, away from the injection position, it furnishes the same results than more precise models but at a lower computational cost. The influence of the convection on the droplets heating and evaporation rate is taken into account using the Ranz–Marshall model.

Within this numerical simulation it was assumed that the droplets dispersion is not influenced by the subgrid turbulence. This assumption is based on the results reported by Fede and Simonin [9]. They showed that the particles dispersion caused by modeled eddies of the flow is very low if $k_c L_f > 10$, where k_c represents the cutoff wave number and L_f is the integral length scale. In the conditions of the present configurations, for a droplet of 10 μm, that is supposed to be the most sensitive to the subgrid velocity fluctuations, the criteria of Fede and Simonin is fully accomplished.

The information exchange between the two phases is performed through a two-way coupling process justified by a volume fraction of the dispersed phase of 7×10^{-5}. The phase coupling between the gas flow and the droplets is achieved by calculating source terms for the mass, momentum and energy transfer during a time interval or cycle. In the cycle n the gaseous phase is computed taking into account the dispersed phase through the source terms computed during the $n-1$ cycle.

3.3. Modeling of the dispersed phase injection

In the current version of the computing code the atomization phenomena is not present. A previous experimental analysis of the spray was performed in non-confined conditions to provide size and velocity of droplets, in particular near the injector. This data provides the boundary conditions for the liquid phase.

The left image from Fig. 2 shows an overview of the numerical injector position and of the droplets velocity vectors in the injection plane. The poly-disperse spray is injected into the flow at 10 mm from the injector. At that distance it can be assumed that the primary atomization process is finished and the droplets are formed. Moreover, the hypothesis of axisymmetry of the spray is still valid, without any perturbation from the turbulent flow. It allows to model the droplets injection by a conical spray.

The repartition of the numerical injection points is uniform. A total number of 640 “elementary injectors”, distributed in 4 elementary rings, was used for the injection of the dispersed phase. In the same image the velocity vectors and mass

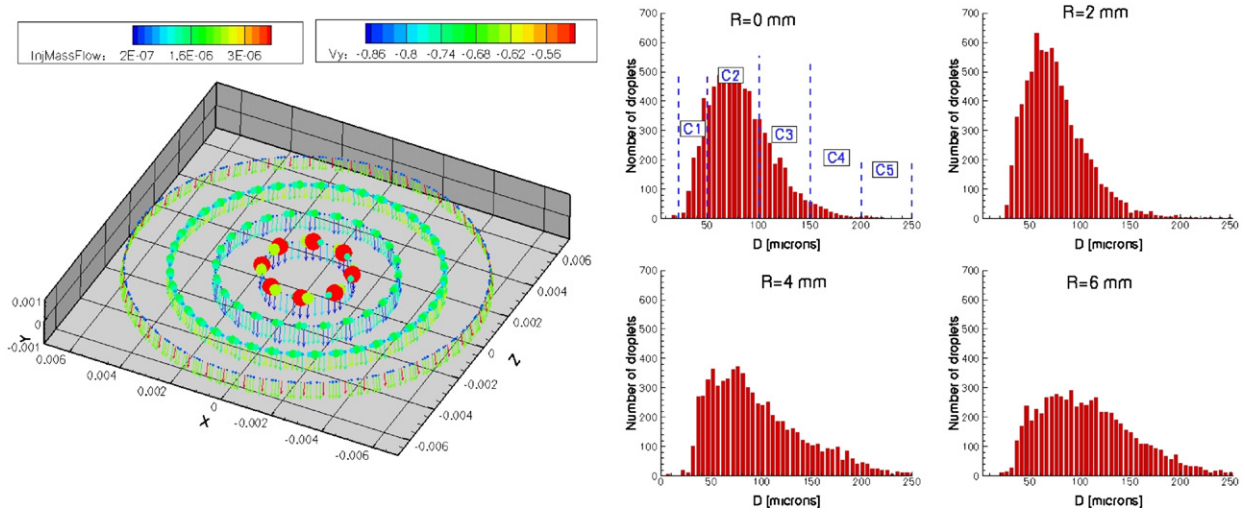

Fig. 2. Left: Example of injection points distribution and velocity vectors. The size of spheres correspond to the mass flow rate of each injection point. Right: Size distributions used for the generation of droplets initial size.

flow rate are plotted for each injector point. To take into account the evolution of size and velocity distributions with the distance from the axis, for each elementary ring a unique size and velocity distribution was used. The experimental size distributions used for the generation of droplets initial conditions are presented in the right side of Fig. 2. Due to the large number of experimental classes of size, a simplification of the real histograms was performed. Hence, it was assumed that a number of 5 numerical classes describe accurately the real distribution. For each numerical class mean values of the droplets size and velocity were calculated. The Stokes number of the injected droplets, calculated on the integral time scale of the gas flow, ranges from 0.05 for the smallest droplets to 5 for the largest one.

4. Results

4.1. Monophase flow

The first test case examines the pure gaseous flow field. For that, a continuous air flow of constant velocity (bulk velocity of 1 m/s in the cross-section channel) and constant temperature (293 K) is imposed through the perforations of the turbulence generator. The walls were kept at the ambient temperature (293 K). The pressure in the channel is the ambient one.

The comparison of numerical results with experimental data carried out in the context of the pure gas phase serves to establish a correct representation of the gaseous flow field used for the subsequent two phase flow simulations.

In a first step the instantaneous behavior of the flow is discussed. The important gas flow features are displayed in Fig. 3, which shows the field of the axial velocity on the mid-plane at $t = 1.35$ s. It corresponds to about 4 residence times in the square cross section channel. The flow topology inside the turbulence generator is characterized by a large, toroidal recirculation zone that follows approximately the geometry of the computational domain. The higher velocity zone enclosing this recirculation zone is created by the 45 micro-jets which impinge onto the walls and the film developing along the convergent walls.

The left image from Fig. 4 depicts the velocity vectors of the jet impinging obliquely the wall at a time $t = 1.35$ s in the mid-plane of the jet. The jet develops from axisymmetric shape near the perforation to a turbulent behavior before impinging the wall. The shear layer between the injected and the ambient fluid is destabilized at half the distance between the injection and the impact point. The vortices emanating from the jet shear layer are clearly seen, as a characteristic of the unsteady behavior. After the flow deflection from the impinging wall, a wall jet develops.

Downstream in the turbulence generator, due to the presence of the recirculation zone, the wall jets grow continuously down to $Y = -40$ mm, where the flow detaches from the wall and does not reattach before leaving the turbulence generator. The effect of the separation phenomenon is to carry vorticity into the global flow due to its very unsteady behavior.

A view of the instantaneous field in the near wake of the injector housing is shown in the right side of Fig. 4. The abrupt geometrical change at the base of the injector housing leads to a flow separation and formation of a recirculation zone. The flow contained within the recirculation zone is dominated by the presence of vortices of different scales.

The geometry of the injector housing and the position of vortices indicate the presence of a deformed ring vortical structure close to the base. This feature fully agrees with the experimental observations performed by Miau [10] behind a circular disc at Reynolds numbers $Re = 10–10^5$. Downstream, due to the high level of turbulence of the upstream flow, the vortical structure is severely distorted.

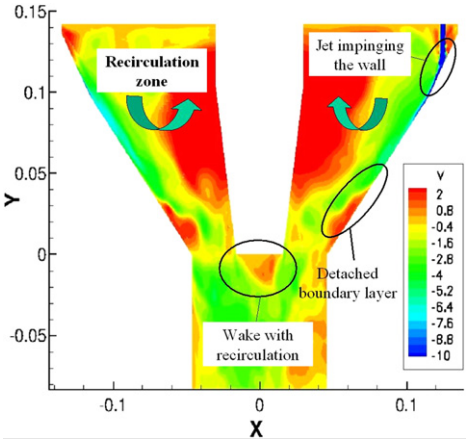

Fig. 3. Instantaneous axial velocity field on the mid-plane at $t = 1.35$ s.

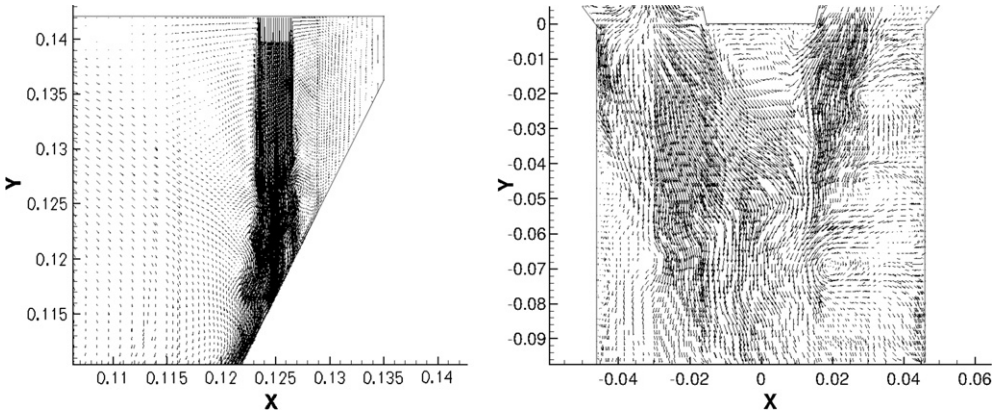

Fig. 4. Instantaneous velocity vectors of the impinging jet (left) and wake of the injector housing (right) in the mid-plane at $t = 1.35$ s.

To check the presence of a dominant structure, during the calculation, the velocity components were recorded by a "virtual" sensor at different locations in the channel. Their positions were selected to be situated outside the shear layer of the wake in order to identify if a particular frequency is present in the flow. It was found that for the longitudinal velocity component, a dominant frequency of ≈ 6.5 Hz is present. It is hypothesized that it is caused by the vortices which are shed when the flow separates from the rear of the injector housing. This frequency corresponds to a Strouhal (St) number of 0.189 which is greater than the Strouhal numbers behind a circular disk (0.134 following [10]).

Following the aspects depicted before, it is believed that, in the square cross-section channel, others vortices are added to the structures generated inside the turbulence generator by the turbulent vortex shedding behind the injector housing.

Once the transient phase is elapsed, temporal averages are computed. Due to the limited computational memory, the strategy adopted to perform the numerical simulation consists in performing calculation for limited intervals of time. The averaged quantities are obtained using a cumulative moving average algorithm. Hence, at the end of every computing interval n ($\Delta t = 0.05$ s), mean velocity fields are computed as:

$$\overline{\mathbf{v}_n^{global}} = \frac{(n-1)\Delta t \cdot \overline{\mathbf{v}_{n-1}^{global}} + \Delta t \cdot \overline{\mathbf{v}_n}}{n \cdot \Delta t} \tag{1}$$

where $\overline{\mathbf{v}_n}$ is the mean velocity computed over the interval n and $\overline{\mathbf{v}_n^{global}}$ is the mean velocity computed over the n intervals.

A long time of integration is required in order to ensure the statistical stationarity of the turbulent flow field, knowing that the larger the sample size is, the more reliable the statistics are. The flow information is collected over 1.82 s (or about 5 residence times in the channel) to get an acceptable level for the mean flow field and various turbulence statistics.

The accuracy of the results is evaluated by comparing them to experimental data. As it was mentioned previously, experimental measurements of the mean and fluctuating velocity in the pure gaseous flow, are available due to the works of M. Cochet [4].

Fig. 5 plots the normalized mean velocity at two downstream locations in the channel. These locations are expressed in dimensionless units Y/H, where $H = 92$ mm represents the width of the channel cross-section. In the upper region of the

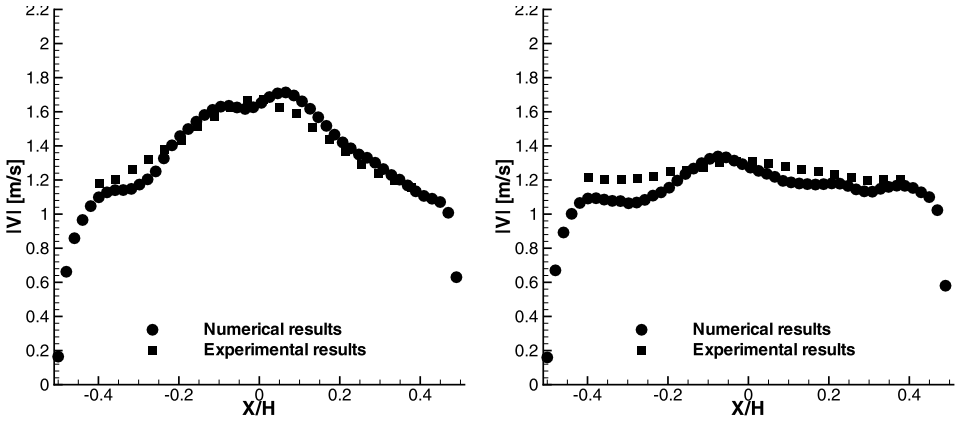

Fig. 5. Mean longitudinal velocity profiles in the channel mid-plane. Left: $|Y|/H = 1$, right: $|Y|/H = 1.5$.

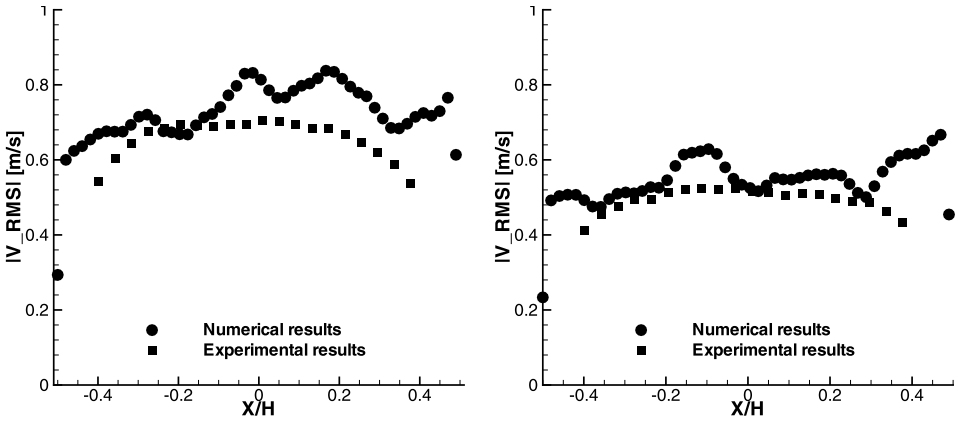

Fig. 6. Transversal profiles of longitudinal velocity fluctuations. Left: $|Y|/H = 1$, right: $|Y|/H = 1.5$.

channel the experimental radial profiles are similar to the longitudinal velocity profiles into a jet. Hence, it can be assumed that, behind the recirculation zone, the shear layers generated at the rear of the injector housing merge together, creating a pseudo-jet. The result is an increase of the longitudinal velocity in the axial region of the channel. The comparison between the numerical and experimental data show small differences.

Fig. 6 gives the profiles of the longitudinal fluctuating velocity. A the good agreement between the simulation and experiment must be noted, even though the limited time of the simulation does not allow to get smooth profiles.

The numerical and experimental axial profiles of the longitudinal mean velocity are compared in Fig. 7. Experimental data, obtained with PIV technique is not available for $|Y|/H < 0.6$. A similar evolution can be found for both simulation and experiment. The differences are inferior to 5% for the longitudinal mean velocity and 8% for the velocity fluctuations.

4.2. Two phase flow

For the second test case the air is pre-heated ($T_{air} = 413$ K) before injection in the turbulence generator. Pure n-octane droplets are injected at $T_{drop} = 285$ K. The other parameters are identical to the first test case.

For the two-phase flow, the analysis of the numerical results is divided in two parts. Firstly, in order to put in evidence the main features of the flow, the instantaneous fields will be discussed. Secondly, comments on the pseudo-Eulerian mean quantities of the dispersed phase will be provided.

4.2.1. Instantaneous two-phase flow topology

A global view of the droplets dispersion in the square cross-section channel is presented in Fig. 8. It depicts an instantaneous image showing all the 196.000 numerical particles at a particular instant when the flow is established. Each numerical particle is represented by a black point. Near the injector, a non-perturbed cloud of droplets can be distinguished, the spray remaining relatively compact. Downstream, the spray is heavily deformed by the structures of the gaseous phase and particles are dispersed across the section of the channel.

Another way of presenting the droplets behavior is to isolate layers of droplets centered into the mid-plane. Such slices of droplets will be used in the following to analyze the droplets temperature and size evolution in the channel.

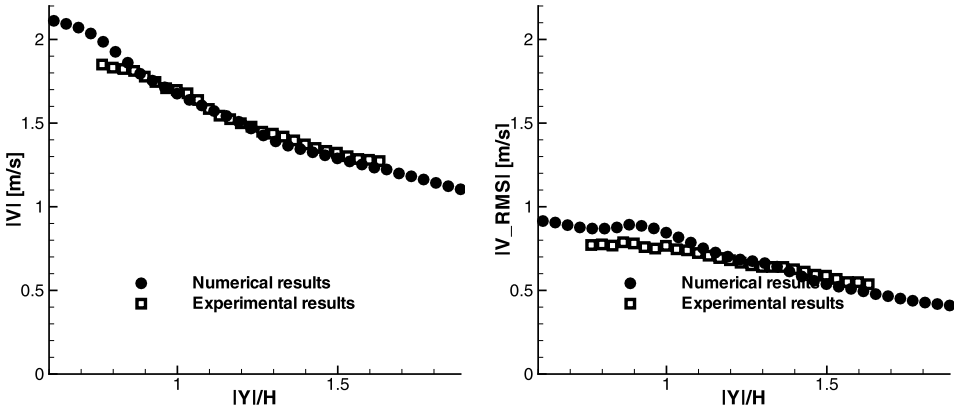

Fig. 7. Axial evolutions of the longitudinal mean velocity and velocity fluctuations.

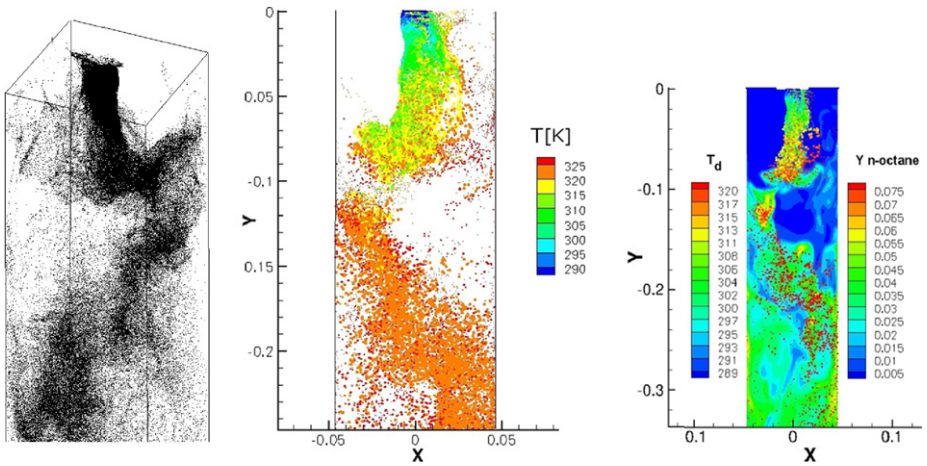

Fig. 8. Left: three-dimensional view of the droplets in the channel. Middle: Instantaneous fields of numerical droplets in the neighborhood of the mid-plane, colored with the droplets temperature and sized by the diameter. Right: Instantaneous field of n-octane vapor concentration and numerical droplets. The temperature is expressed in K and the vapor concentration in volume fractions.

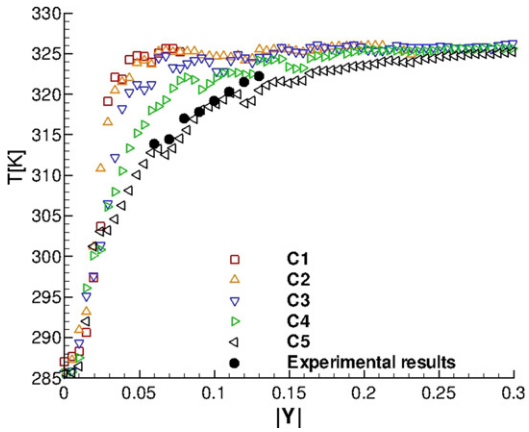

Fig. 9. Axial evolution of the droplet temperature. The classes are defined as follows: C1 – 25 μm $< d_0 <$ 50 μm, C2 – 50 μm $< d_0 <$ 100 μm, C3 – 100 μm $< d_0 <$ 150 μm, C4 – 150 μm $< d_0 <$ 200 μm, C5 – 200 μm $< d_0 <$ 250 μm.

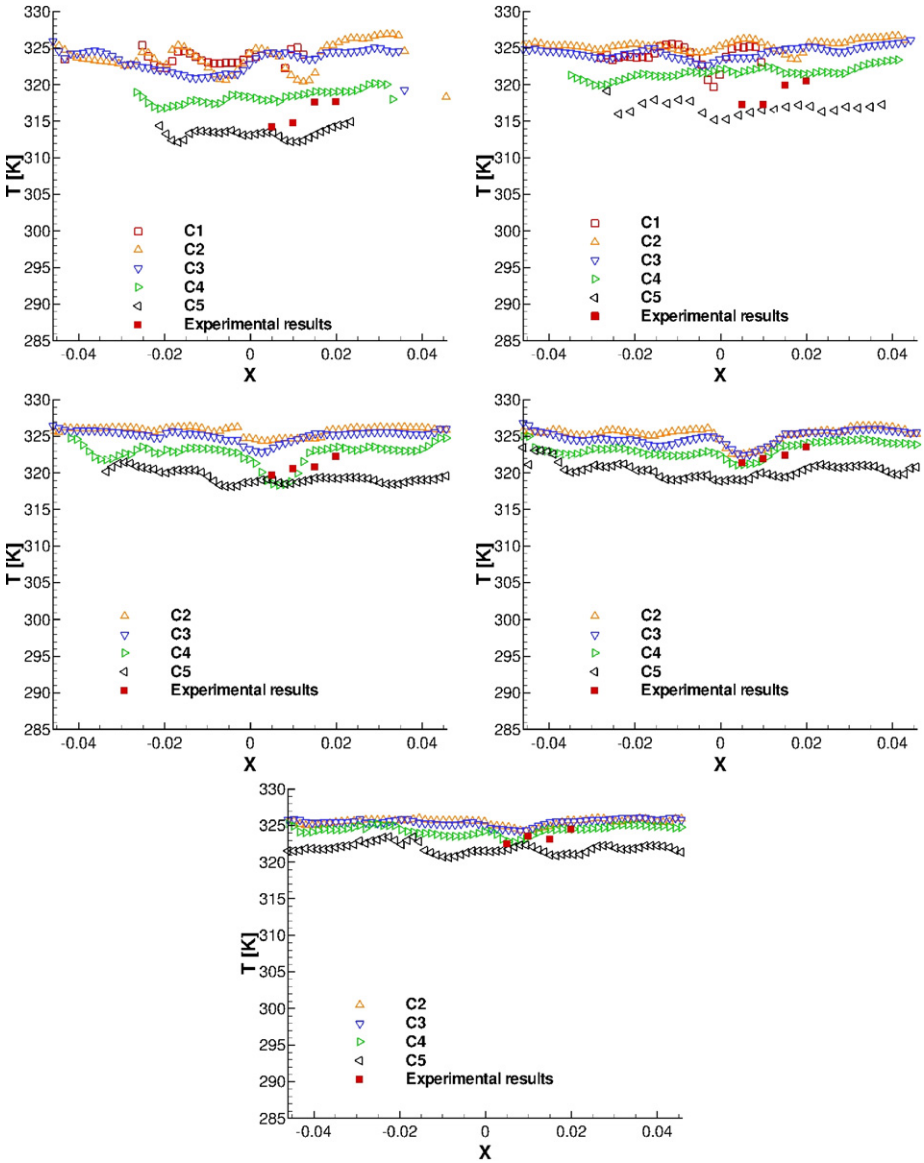

Fig. 10. Radial evolution of the droplet temperature. Top-left: $Y = -60$ mm, top-right: $Y = -80$ mm, middle-left: $Y = -100$ mm, middle-right: $Y = -120$ mm, bottom: $Y = -140$ mm.

The droplet heat transfer is an important aspect of the evaporation process. As a large difference exists between the air and the droplets at the entrance of the channel, the liquid phase is characterized by an important heating, until an equilibrium temperature is reached. This evolution can be observed on the visualization of the droplets temperature (middle image from Fig. 8). In the upper region of the spray (-100 mm $< Y < 0$ mm), the droplets temperature continuously increases. The equilibrium temperature of about 325 K is reached between $Y = -100$ to -150 mm. Downstream, the droplet temperature is nearly constant throughout the volume of the channel. The temperature evolution between the injection and the equilibrium state depends on the droplet sizes. Hence, the small droplets heat faster than the largest ones. Additionally, the droplets from the borders of the spray tend to heat faster due to their entrainment into regions of flow of higher temperature. This mechanism is obvious in the first zone of the channel $Y > -100$ mm.

The evaporation process inside the channel is characterized by coupling effects between the gas and the liquid phases. The mass transfer is the most important phenomenon which occurs during evaporation. It contributes to the modification of the composition of the gas in the channel. The instantaneous field of n-octane vapor is shown in the right image of Fig. 8 together with the numerical droplets as they appear in the carrier flow. In the first part of the channel ($Y > -150$ mm) an important spatial heterogeneity in vapor concentration must be noted. The high vapor concentration regions alternate with regions with less important values of concentration. The simultaneous presentation of gaseous and liquid phases allows to

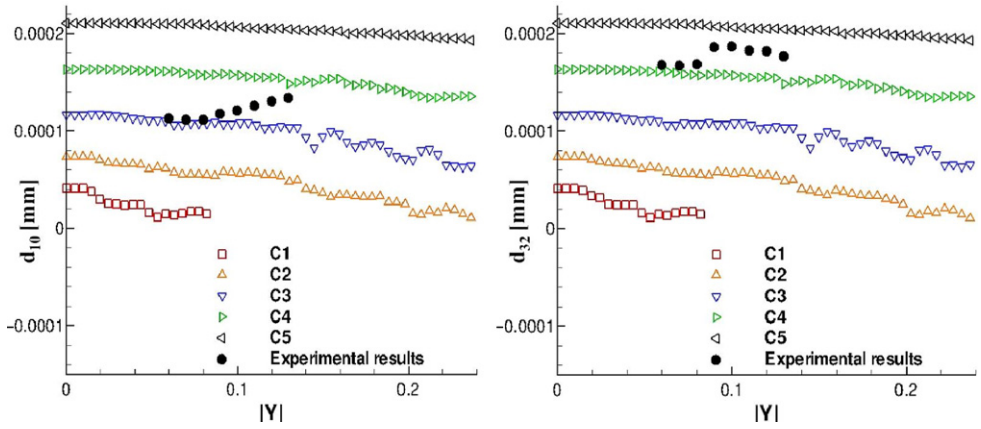

Fig. 11. Axial evolution of the droplet size.

conclude that droplets and vapor follow together the coherent structures of the turbulent flow. In addition, the distribution of the vapor wake indicates the trajectory of the cloud of droplets.

4.2.2. Comparison between experimental and numerical data

Although the previous visualizations provide useful information about the droplet behavior in the flow, exploitable values are difficult to be obtained. For a more precise analysis of the droplets temperature, velocity and size evolution, average quantities must be calculated. From a numerical point of view, these quantities are reconstructed by averaging over all droplets present in a given computing cell. Furthermore, to get the temporal averaged values, the resulting pseudo-Eulerian instantaneous fields are processed with an exponential moving average technique. The grid cells without droplets have been neglected in the processing of averages. To compute the mean values, the transient phase is not considered, only the last 1.8 s of the simulation being taken into account. This period of time corresponds to approximately 5 residence times in the channel, where the residence time is calculated as the ratio of the channel length to the bulk velocity.

The axial evolution of the droplet mean temperature for each class of size is presented in Fig. 9. The droplets heating along the channel axis is obvious. The increase of the droplets temperature proves that the droplets are still in the heating phase in the investigated region of the channel. As it was expected, the heating of the smaller droplets is faster than for the larger ones. Numerical results are compared with the experimental data obtained with Global Rainbow Refractometry technique. There is a qualitative agreement between the experimental and numerical evolutions. In the first part of the channel, the experimental values are closer to the numerical values corresponding to the largest droplets (class C5). An explanation of this behavior can be given by the experimental measurement technique. It is possible that only the light diffused by the large droplets contributes to the formation of the global rainbow signal, the measured temperature corresponding to the temperature of large droplets.

Fig. 10 presents the radial change in the droplet temperature for different axial positions. We note the existence of a radial temperature gradient that is more important closer to the injector. At short distances from the nozzle tip the spray expansion is fairly narrow and the droplets are not yet fully dispersed by the continuous phase. Thus, the heat exchange is more important at the borders of the spray. Downstream, the temperature tends to be more homogeneous due to the turbulent dispersion of droplets over the section of the channel.

Fig. 11 presents the axial evolutions of the mean diameter d_{10} and d_{32} for each class. The evaporation of droplets is clear because their diameter decreases along the channel axis for all classes. Moreover, the droplets from the first class C1 evaporate completely in the first 100 mm, while the class C2 is completely evaporated at about 240 mm. A direct result of the disappearance of these classes is the increase of the global mean diameter d_{10} and d_{32}. Qualitatively, the same result is obtained experimentally [5] using the PDA system. Both experimental profiles of d_{10} and d_{32} change the slope at about $Y = -90$ mm. This evolution may be explained only by the complete evaporation of small droplets in this region of the channel.

5. Conclusions

In order to evaluate the implementation of the evaporation models in the ONERA CFD code, an Eulerian–Lagrangian simulation was performed at the ambient pressure for a n-octane poly-disperse spray evaporating in a fully turbulent heated flow.

The flow configuration and operating parameters allowed to partially recreate the flow conditions inside a turbojet combustor. An experimental database previously created in collaboration with F. Moreau and M. Cochet from Fluids Mechanics Institute of Toulouse was used to test the evaporation models implemented in the CEDRE code.

The instantaneous and averaged flow fields obtained allowed to put in evidence some features in the dispersed phase flow such as the droplets evaporation and turbulent dispersion. The description of the dispersed phase seems consistent with the experiment. Comparison of numerical and experimental data showed that the values are in a relative good agreement in spite of the limited time of simulation.

Further investigations will consider evaporation of multicomponent droplets.

References

[1] N. Doué, Modélisation de l'évaporation de gouttes multicomposants, PhD Thesis, Institut Supérieur de l'Aéronautique et de l'Espace, 2005.
[2] C. Laurent, Développement et validation de modéles d'évaporation multi-composant, PhD Thesis, Institut Supérieur de l'Aéronautique et de l'Espace, 2008.
[3] V. Bodoc, J. Wilms, Y. Biscos, G. Lavergne, Experimental and numerical investigation of a monocomponent polydisperse spray, in: Proceedings of ILASS Conference, 2008.
[4] M. Cochet, Évaporation de gouttelettes polydispersés dans un écoulement de canal fortement turbulent. Analyse de la formation du mélange diphasique par imagerie de fluorescence, PhD Thesis, Institut National Polytechnique de Toulouse, 2007.
[5] F. Moreau, Évaporation et dispersion d'un spray bi-composant dans un écoulement de canal chauffé fortement turbulent. Une approche expérimentale, PhD Thesis, Institut National Politechnique de Toulouse.
[6] V. Bodoc, F. Moreau, Yves Biscos, R. Basile, G. Lavergne, Experimental investigation of evaporating bi-component droplets in a turbulent channel flow, in: Proceedings of ICLASS Conference, 2009.
[7] F. Beaubert, S. Viazzo, Large eddy simulations of plane turbulent impinging jets at moderate Reynolds numbers, International Journal of Heat and Fluid Flow 24 (2003) 512–519.
[8] I.B. Ozdemir, J.H. Whitelaw, Impingement of an axisymmetric jet on unheated and heated flat plates, Journal of Fluid Mechanics 240 (1992) 503–532.
[9] P. Fede, O. Simonin, Numerical study of the subgrid fluid turbulence effects on the statistics of heavy colliding particles, Physics of Fluids 18 (2006).
[10] J.J. Miau, T.S. Leu, T.W. Liu, J.H. Chou, On vortex shedding behind a circular disk, Experiments in Fluids 2 (1997) 225–233.